Ultrahigh Torsional Stiffness and Strength of Boron Nitride Nanotubes

Jonathan Garel,[†] Itai Leven,[‡] Chunyi Zhi,[§] K.S. Nagapriya,[†,⊥] Ronit Popovitz-Biro,[‖] Dmitri Golberg,[§] Yoshio Bando,[§] Oded Hod,[‡] and Ernesto Joselevich,[†]*

[†]Department of Materials and Interfaces, Weizmann Institute of Science, Rehovot 76100, Israel

[‡]School of Chemistry, The Sackler Faculty of Exact Sciences, Tel Aviv University, Tel Aviv 69978, Israel

[§]International Center for Materials Nanoarchitectonics (MANA), National Institute for Materials Science (NIMS), Namiki 1-1, Tsukuba, Ibaraki 305-0044, Japan

[‖]Chemical Research Support, Weizmann Institute of Science, Rehovot 76100, Israel

*email: ernesto.joselevich@weizmann.ac.il

Table S1: BNNT torsional mechanical characterization.

BNNT #	d (nm)	L (nm)	κ (10^{-14} N.m)	G_s (GPa)	G_h (GPa)	τ_{BNNT} (GPa)
A	10.5 ± 0.3	100 ± 10	0.17 ± 0.07	130 ± 60	530 ± 220	
B	10.7 ± 0.9	100 ± 20	0.25 ± 0.07	190 ± 80	770 ± 290	
C	13.4 ± 1.1	170 ± 30	0.9 ± 0.3	460 ± 180	2300 ± 800	
D	17.6 ± 0.7	320 ± 10	1.2 ± 0.2	420 ± 80	2600 ± 500	
E	17.8 ± 1.5	380 ± 10	0.6 ± 0.2	210 ± 90	1400 ± 600	
F	18.5 ± 1.0	420 ± 10	0.8 ± 0.2	300 ± 70	2100 ± 500	
G	21.6 ± 1.4	290 ± 30	1.3 ± 0.3	180 ± 50	1400 ± 400	> 0.8
H	22.4 ± 0.8	210 ± 10	3.1 ± 0.5	260 ± 50	2200 ± 400	> 2.0
I	22.8 ± 0.6	350 ± 10	1.6 ± 0.2	210 ± 40	1800 ± 300	
J	25.4 ± 1.2	320 ± 10	4.3 ± 0.7	340 ± 80	3200 ± 700	
K	26.0 ± 2.2	330 ± 10	3.3 ± 0.8	240 ± 80	2300 ± 800	> 1.3
L	27.7 ± 1.0	370 ± 10	2.3 ± 0.3	150 ± 30	1500 ± 300	
M	29.6 ± 2.6	180 ± 20	3.5 ± 0.2	82 ± 20	910 ± 180	
N	30.2 ± 2.4	280 ± 10	1.7 ± 0.3	58 ± 14	660 ± 150	
O	32.6 ± 0.7	360 ± 20	1.1 ± 0.2	36 ± 9	440 ± 110	
P	39.2 ± 2.0	290 ± 30	6 ± 2	63 ± 27	920 ± 390	
Q	42.8 ± 3.6	280 ± 20	4.9 ± 0.7	41 ± 10	660 ± 150	

d: BNNT diameter; L: BNNT suspended length (obtained both from AFM topography); κ: torsional spring constant; G_s and G_h: effective shear moduli according to solid rod and hollow cylinder model, respectively; τ_{BNNT}: torsional strength (calculated for the whole nanotube). The experimental error (EE) for d is the standard deviation of several measurements performed along the BNNT length. The EE for L is derived from the resolution of the AFM topography image. The EE for κ is the damped least-squares fitting error obtained by fitting linear stiffness versus lever arm plots (Figure 1d and Figure S1) to equation (1) (see text and Methods below). The EE for G_h and G_s is obtained by combining the EE for d, L and κ.
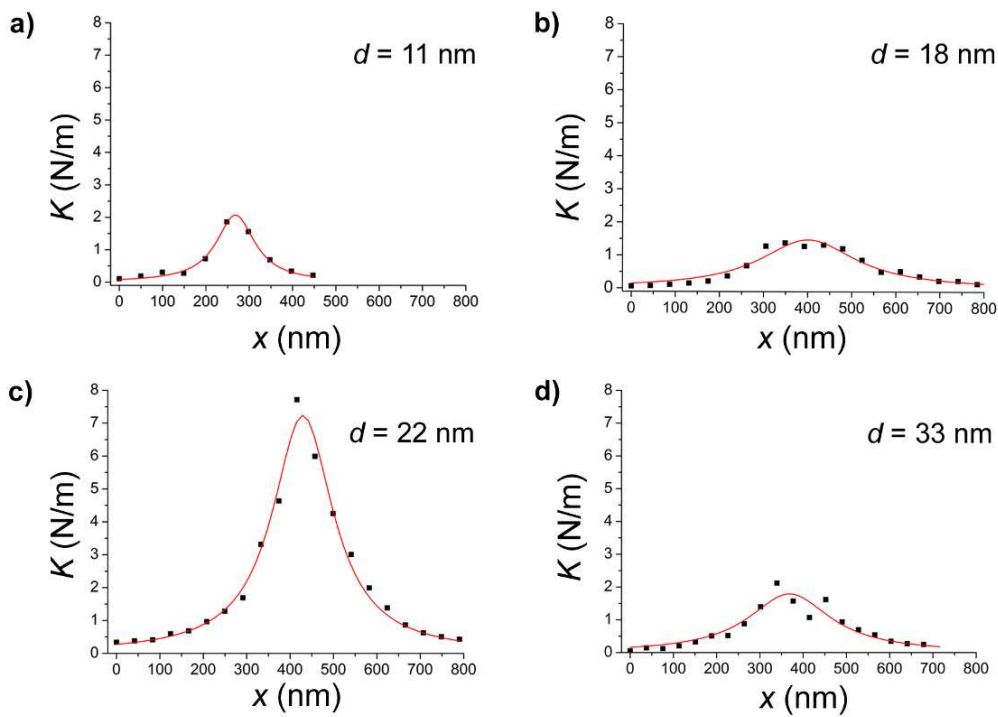
Figure S1: Additional plots of linear stiffness against lever arm, for nanotubes B **(a)**, D **(b)**, H **(c)** and O **(d)**. x represents the position along the pedal (the first measurement point is set to zero by definition). The data were fitted to equation (1) (see text).
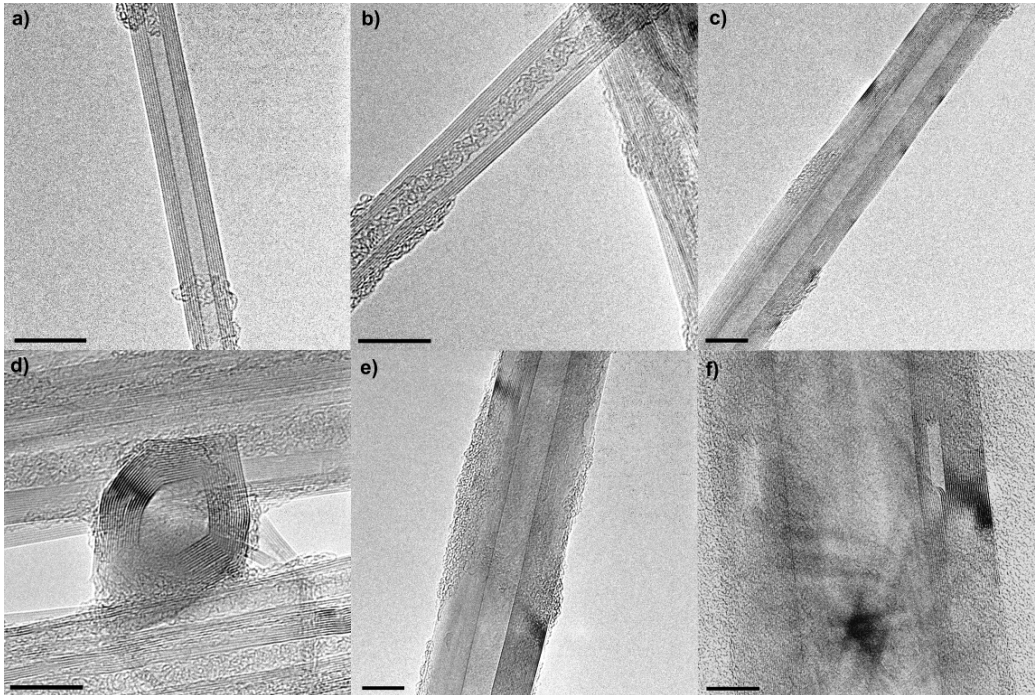
Figure S2: BNNTs of different diameters and cross-section geometry. TEM images of BNNTs of diameters 7 nm **(a)**, 9 nm **(b)**, 16 nm **(c)**, 22 nm **(d)**, 25 nm **(e)**, and 37 nm **(f)**. Whereas nanotubes **(a)** and **(b)** have circular cross-sections, the black areas visible in nanotubes **(c)**, **(e)** and **(f)** are a known indication of faceting. The faceted nature of nanotube **(d)** can be demonstrated by a direct observation of its polygonal cross-section. All scale bars: 10 nm.

Methods

Synthesis: BNNT were synthesized by chemical vapor deposition as described in [S1] (nanotubes A to C) and [S2] (nanotubes D to Q).

Nanofabrication: The torsional BNNT-based NEMS were produced by methods similar to those reported for previous torsional devices.[S3-S5] Alignment marks were created on thermally oxidized silicon wafers (Si<100>, oxide thickness: 1μm) by electron-beam lithography, metal evaporation and lift-off. BNNTs were dispersed in 1,2-dichloroethane by brief sonication prior to deposition. BNNTs tend to agglomerate as bundles and could not be fully separated by sonication. To produce individual nanotubes, BNNT aggregates were deposited on the Si wafer, which was then flushed with acetone and isopropanol, leaving behind several well separated nanotubes suitable for device production. The nanotubes were mapped and their diameter was measured by AFM imaging. Pads and pedals were laid down respectively onto the ends and middle part of the selected BNNTs by electron beam lithography, electron beam evaporation of Cr (5 nm) and Au (80 nm), and lift-off in acetone. The SiO_2 layer was then etched in aqueous HF/NH_4F (1:6) for 7 minutes. Then, without drying the samples, the etching solution was consecutively replaced by water, ethanol and pressurized CO_2, from which they were critical-point dried. Devices A, B and C (Supplementary Table 1) were grounded during the torsion experiment, which required additional fabrication steps. Large electrodes were written

by electron-beam lithography together with pads and pedals. Then, before etching the SiO$_2$ layer, the sample was mounted into a chip carrier and wire-bonded.

BNNT torsion measurements: AFM imaging and mechanical measurements were performed on a Veeco Multimode/Nanoscope V equipped with a closed-loop scanner.

The device on which we wish to perform the torsion experiment is first imaged in tapping mode (TM) AFM. We then zoom at the desired position and press on the pedal with the AFM tip, which twists the nanotube. During each press cycle, we acquire measurements of both the oscillation amplitude of the cantilever and its TM deflection as a function of its z-position ("force-distance measurement"). The TM deflection plot records the deformation of the cantilever as it presses on the pedal, whereas the amplitude plot is used as a control: when the tip touches the pedal, the oscillation amplitude of the cantilever is supposed to reach zero. Before the experiment itself, we always perform a force-distance measurement on a hard Au surface as a calibration (Figure S3). In order to get meaningful data, we need the spring constant of the cantilever to be of the same order of magnitude as the apparent spring constant of the nanotube. In most cases, 70 kHz silicon tips (Olympus) with a spring constant of ~ 2 N/m were successfully used; for devices A, B and C, we used low-frequency cantilevers (Micromasch, ν = 20 kHz, k_c = 0.3 N/m). All spring constants were recalibrated by thermal tuning method. Additionally, the whole experiment is conducted under dry N$_2$ flow in order to reduce humidity and thermal fluctuations. For thin BNNT devices (devices A, B and C), both the tip and the device were grounded during the experiment, in order to avoid static charging, which could break the device through electrostatic forces.
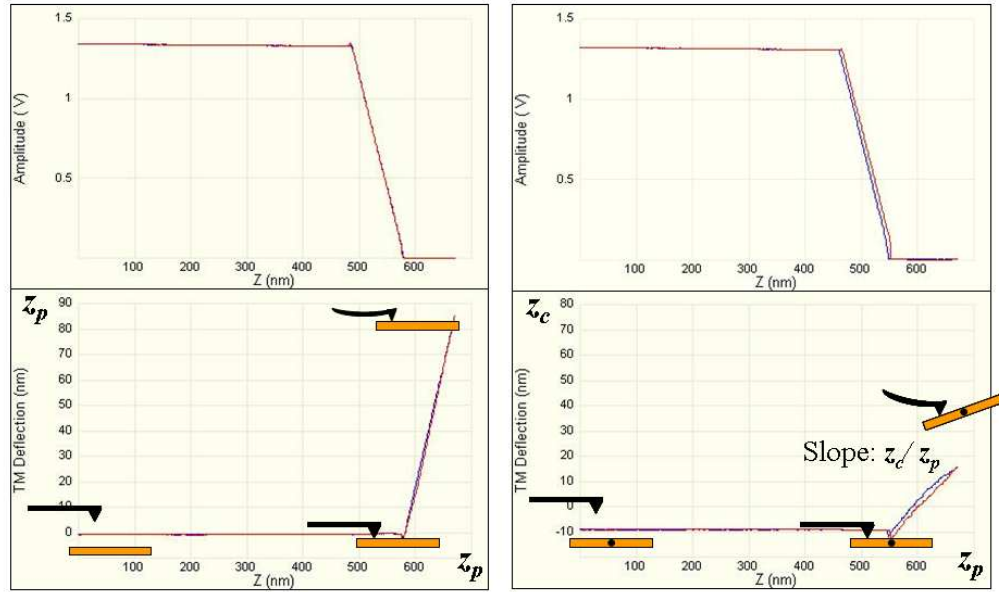
Figure S3: Force-distance measurements recorded upon pressing on a hard surface (left) and on the pedal (right). In both cases, when the tip touches the surface, the tapping amplitude reaches zero. The tapping mode deflection then increases linearly, corresponding to cantilever deformation. Because the pedal twists, the deformation undergone by the cantilever is less significant than if pressing on a hard surface, hence the smaller slope. In blue: trace; in red: retrace.

The torsional stiffness was measured by pressing at a series of points along the pedal as described in the text, in Figure 1d, and in Supplementary Figure 1. Since k_c, z_p and z_c (see text) can all be determined with accuracy < 2%, the major source of uncertainty on κ comes from the experimental fit. Additionally, we were cautious to reach only low torsion angles (< 20°), in order to avoid any non-linear response, or plastic transition, which could arise at higher torsion angles. In most cases, the measurements were repeated either immediately, or a few weeks after the first

7

experiment. The values measured for κ were found to be identical within the margin of experimental error. This indicates that no plastic irreversible transition has occurred, and that the true elastic torsional spring constant of each BNNT device is obtained.

We were concerned that the metallic pedal might undergo deformation upon pressing, thus leading to an underestimation of the torsional spring constant. To test this possible effect, we built several "diving boards" (cantilevers extending from the metallic pads) and pressed along the board at regular intervals while acquiring force-distance measurements. We then plotted the stiffness as a function of the distance from the edge (Figure S4). It is visible that while the stiffness indeed decreases along the board, thus indicating that it undergoes deformation, the board always remains much stiffer than the "pedal + nanotube" system. We could measure the apparent torsional spring constant of the board to be $\kappa_{Au} = 1.9 \pm 0.1 \cdot 10^{-12}$ N·m, which is one to two orders of magnitude larger than the typical spring constant of a multiwall BNNT. Therefore, in most cases, the elasticity of the Au pedal was negligible. When deemed necessary, we corrected the nanotube torsional spring constants accordingly.
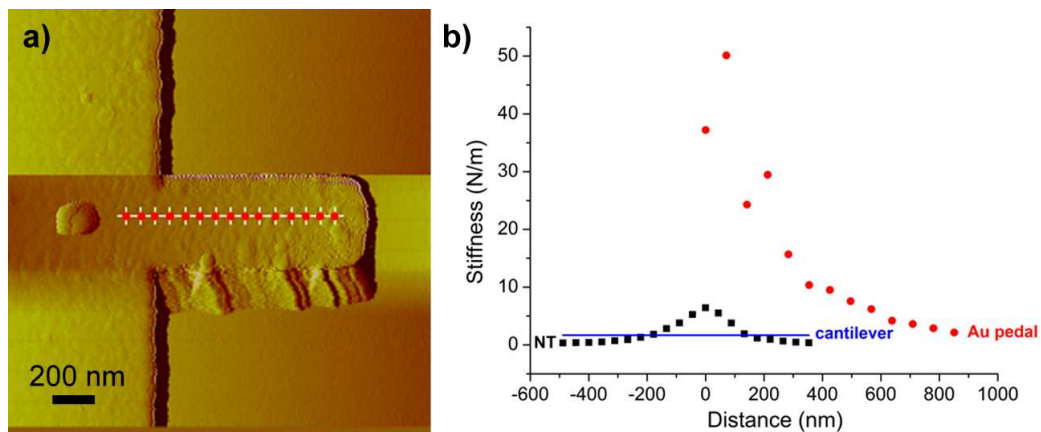
Figure S4: Pedal deformation. (a) AFM tapping mode image of a suspended "diving board". For every position marked with a red dot, we acquired a force-distance measurement. **(b)** Relative stiffness of a BNNT (black) compared to Au pedal (red) and AFM cantilever stiffness (blue), as a function of distance from the torsional axis. Whereas the nanotube and cantilever stiffness are of the same order of magnitude, the Au pedal is one to two orders of magnitude stiffer.

Microscopy: SEM imaging was performed with a Supra 55VP FEG LEO Zeiss in ultra-high vacuum, at acceleration voltage 5 kV. TEM imaging was performed on a FEI/Philips CM120, at acceleration voltage 120 kV.

Modeling

1. <u>Registry index for a faceted double walled boron nitride nanotube</u>

A faceted achiral double walled boron nitride nanotube (DWBNNT) has a polygonal cross-section which can be represented as follows (we use a perfect hexagonal cross section as an example):
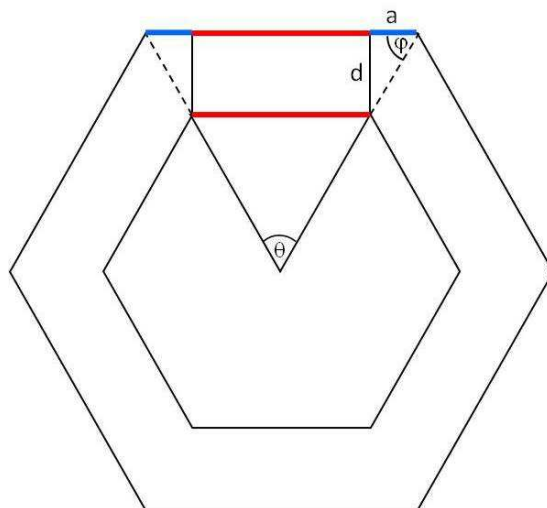
Figure S5: Model for a faceted nanotube with a hexagonal cross section

We identify two types of regions along the polygonal circumference: (i) Side regions where sections of the outer prism can be projected onto parallel sections of the inner prism (we shall name these sections as "red" sections as they are marked with bold red lines in the above figure) (ii) Apex regions where such projections are not possible (these sections will be named as blue sections as they are marked with bold blue lines

in the figure). The length of each of the "blue" apex section is $a = d / \tan\varphi$ where $d \approx$ 3.33 Å is the interlayer separation. The angle φ is related to the central angle $\theta = 2\pi/n$, and thus to the number of apexes n, via $\varphi = \dfrac{\pi - \theta}{2} = \pi\left(\dfrac{1}{2} - \dfrac{1}{n}\right)$. Using these relations we find that the total length of the "blue" sections of the outer shell is given by

$$2an = \frac{2dn}{\tan\left[\pi\left(\dfrac{1}{2} - \dfrac{1}{n}\right)\right]}.$$

The overall circumference of the outer shell L is assumed to be equal to the circumference of the corresponding pristine tube namely, $L = \pi D$, D being the diameter of the non-faceted outer tube. Therefore, the portion of the circumference that is of "red" type:

$$\beta = \frac{L - 2an}{L} = 1 - \frac{2dn}{\pi D \tan\left[\pi\left(\dfrac{1}{2} - \dfrac{1}{n}\right)\right]}$$

For the calculation of the registry index we now assume that the "red" sections are in perfect registry and thus contribute "-1" to the overall registry index and the "blue" sections which have no interlayer overlap are "neutral" in terms of their registry mismatch and thus contribute "0" to the overall registry. Thus the registry index can now be evaluated as:

$$RI_{Facetted} = (-1) \cdot \beta + (0) \cdot (1 - \beta) = -\beta = \frac{2dn}{\pi D \tan\left[\pi\left(\dfrac{1}{2} - \dfrac{1}{n}\right)\right]} - 1$$

It should be noted that in order to obtain perfect registry in the "red" regions the difference in length between the inner and outer facet which is of length $2a$ should be

integer multiples of the unit cells translational vector along the nanotube circumference. Naturally, this condition is hard to achieve and therefore one should expect that the "blue" regions will be somewhat stressed to allow for enhanced registry in the "red" regions which will not be in perfect registry.

Figure 4d presents the results of this model for a hexagonal cross section. The dependence of the registry index, calculated using the above described procedure, on the number of apexes of the faceted nanotubes is plotted in Figure S6.
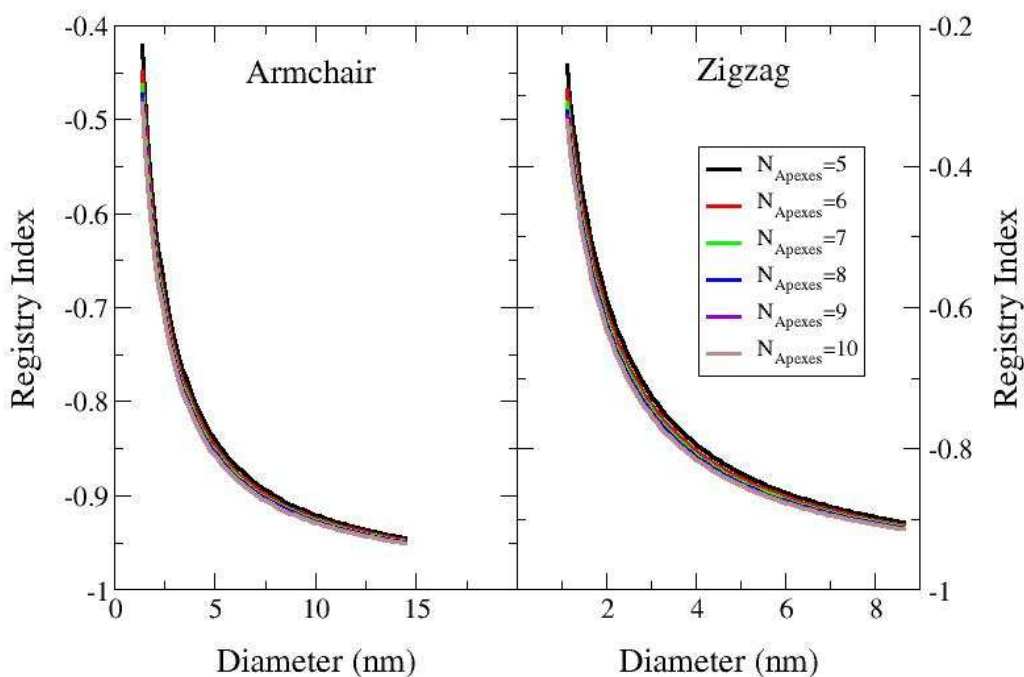
Figure S6: Dependence of the registry index of a faceted BNNT, calculated using the procedure described above, on the number of apexes of the faceted nanotubes. Left panel: armchair DWBNNTs; Right panel: zigzag DWBNNTs. As can be seen, the dependence of the calculated RI on the number of apexes is relatively weak thus justifying our use of a hexagonal cross section.

12

2. <u>Scaling of torsional mechanical coupling with BNNT radius</u>

TEM imaging indicated that faceting is the origin of the ultrahigh torsional stiffness observed in multiwall BNNTs. Based on the observation that thick BNNTs appear faceted in TEM and yet exhibit weak torsional coupling, we hypothesized that thick BNNTs undergo unfaceting upon twisting: under torsion, some (or all) shells of a thick BNNT undergo a conformational change that allows the outer layer(s) to slide freely.

The model we develop addresses the two following questions:

(i) What drives the formation of facets, and why do they appear only above a certain diameter?

(ii) What drives the unfaceting of faceted nanotubes? Why is it favored for thicker tubes?

This model is based primarily on analyzing how each contribution to the BNNT total energy scales with the BNNT radius R.

2.1. Formation of facets

The faceting of the nanotubes, namely the transition between circular and faceted cross sections, results from a delicate balance between intralayer and interlayer energy contributions. We will now evaluate the scaling with R of intralayer and interlayer effects both for cylindrical and faceted nanotubes.

2.1.1. Intralayer energy

The intralayer energy for circular nanotubes corresponds to the curvature strain energy E_{curv}. E_{curv} scales linearly with the number of layers, and quadratically with the curvature of the nanotube.[S6] The number of layers scales with R and the curvature scales with R^{-1}, therefore $E_{curv} \propto R^{-1}$.

The intralayer energy for faceted nanotubes corresponds to the energy required to create facet edges. E_{edges} is proportional to the total number of edges. The number of edges per layer being a constant, E_{edges} therefore increases linearly with the number of layers: $E_{edges} \propto R$.

2.1.2. Interlayer energy

The interlayer energy corresponds to the attraction (or repulsion) felt by an atom from its nearest out-of-plane neighbors. The total interlayer energy E_{inter} is the sum of these individual contributions over the whole nanotube. E_{inter} therefore scales like the nanotube cross-section area, i.e. $E_{inter} \propto R^2$, both for circular and faceted nanotubes.

E_{inter} also depends on the stacking between the layers: the better the stacking, the lower (i.e. the more stabilizing) E_{inter} will be. Or, expressed in terms of registry index (RI) (see Figure 4d): the lower the RI, the lower E_{inter}. Figure 4d shows that for a diameter d > 2-3 nm, the RI is lower for faceted than for circular nanotubes. One can therefore safely assume that for our BNNTs, E_{inter} is lower for faceted than for

circular nanotubes. Moreover, the RI saturates and does not vary with d when d becomes larger than a few nm.

2.1.3. Total energy

One can now express the total energy of the nanotube, both in the faceted and the circular geometry. For circular nanotube, the total energy E^C can be written as

$$E^C(R) = E^C_{inter}(R) + E^C_{intra}(R) = \alpha R^2 + \beta R^{-1}$$

where α and β are independent of R. Similarly, for faceted nanotubes:

$$E^F(R) = E^F_{inter}(R) + E^F_{intra}(R) = \alpha' R^2 + \beta' R$$

where α' and β' are independent of R. We have also established that $E^F_{inter} < E^C_{inter}$ and therefore $\alpha' < \alpha$. As R increases, interlayer contributions, which scale like R^2, become dominant over intralayer contributions, which scale like R or R^{-1}. Since $E^F_{inter} < E^C_{inter}$, the energy of the faceted geometry becomes lower than the energy of the cylindrical geometry above a certain R_F (faceting radius): the nanotube undergoes faceting. In other words, when the nanotube becomes large enough, it can create large flat areas with perfect registry that compensate for the energetical cost of edges; then faceting occurs.

2.2. Unfaceting under torsional stress

Upon application of a torque, a third energy contribution must be considered: the elastic torsional energy E_{twist}. Let us now evaluate the scaling of E_{twist} with R in the

two extreme cases described in the main text of the article (one layer twisting and slipping vs. all layer twisting together).

One layer twisting: $E_{twist\text{-}one} = (1/2)\kappa_{one}\phi^2$ where $\kappa_{one} = (4G\pi R^3 \delta r)/(2L)$: $E_{twist\text{-}one} \propto R^3$.

All layers twisting: $E_{twist\text{-}all} = (1/2)\kappa_{all}\phi^2$ where $\kappa_{one} = (G\pi R^4)/(2L)$: $E_{twist\text{-}all} \propto R^4$.

Therefore, torsional energy terms, which scale at least as R^3, are expected to become dominant over both intra- and interlayer energy terms (scaling at most as R^2) as R increases. Since $E_{twist\text{-}one} \propto R^3$ and $E_{twist\text{-}all} \propto R^4$, slipping of the outer layer around the inner shells should become favorable for large R – even at the expense of significant internal reorganization and increase of the interlayer energy. In other words: above a certain R_U (unfaceting radius) and submitted to a torsional stress, the faceted nanotube reverts back to a circular geometry, thereby allowing its outer shell to freely slide around its inner layers. It should be noted that unfaceting is also expected to occur below R_U if the torsion angle is large enough, which probably accounts for the relative softening observed at large twisting angles in Figure 3.

2.3. Summary

We have shown here that the various torsional behaviors observed for BNNTs are due to a delicate balance of their intralayer, interlayer and torsional energies.

For thin nanotubes, intralayer energy dominates: the energetical cost of facet edges is too heavy and thin BNNTs are thus circular. They exhibit a low torsional coupling and low sliding energy, due probably to the loss of commensurability between layers arising when h-BN folds into BNNTs.

16

For **intermediate nanotubes, interlayer energy dominates**: interlayer stabilization allows the formation of faceted nanotube, and the preservation of the faceted structure upon twisting. A large torsional coupling ("ultrahigh stiffness") is observed.

For **thick nanotubes, torsional energy dominates**, entailing unfaceting of the nanotube to allow the outer shell to slip around the inner layers. The torsional coupling is again low.

Supplementary references

S1.   Huang, Y.; Lin, J.; Tang, C. C.; Bando, Y.; Zhi, C. Y.; Zhai, T. Y.; Dierre, B.; Sekiguchi, T.; Golberg, D. *Nanotechnology* **2011,** *22,* 145602.

S2.   Tang, C.; Bando, Y.; Sato, T.; Kurashima, K. *Chem. Commun.* **2002**, 1290-1291.

S3.   Cohen-Karni, T.; Segev, L.; Srur-Lavi, O.; Cohen, S. R.; Joselevich, E. *Nature Nanotechnol.* **2006,** *1*, 36-41.

S4.   Nagapriya, K.; Berber, S.; Cohen-Karni, T.; Segev, L.; Srur-Lavi, O.; Tománek, D.; Joselevich, E. *Phys. Rev. B* **2008,** *78,* 165417

S5.   Nagapriya, K.; Goldbart, O.; Kaplan-Ashiri, I.; Seifert, G.; Tenne, R.; Joselevich, E. *Phys. Rev. Lett.* **2008,** *101,*195501.

S6.   Srolovitz, D.; Safran, S.; Tenne, R. *Phys. Rev. E* **1994,** *49*, 5260-5270.